APL Photonics

RESEARCH ARTICLE | SEPTEMBER 19 2023

Wideband image-reject RF channelization based on soliton microcombs (invited paper)

Special Collection: State-of-the-Art and Future Directions in Optical Frequency Comb Sources, Enabling Technologies, and Applications

Jiewen Ding ; Yifan Wu ; Huashan Yang ; Chao Zhang ; Yifei Zhang ; Jijun He ; Dan Zhu ; Shilong Pan

APL Photonics 8, 090801 (2023)
https://doi.org/10.1063/5.0165848

AIP Publishing

Wideband image-reject RF channelization based on soliton microcombs (invited paper)

Cite as: APL Photon. 8, 090801 (2023); doi: 10.1063/5.0165848
Submitted: 30 June 2023 • Accepted: 28 August 2023 •
Published Online: 19 September 2023

Jiewen Ding, Yifan Wu, Huashan Yang, Chao Zhang, Yifei Zhang, Jijun He,[a] Dan Zhu,[a] and Shilong Pan[a]

AFFILIATIONS

National Key Laboratory of Microwave Photonics, Nanjing University of Aeronautics and Astronautics, Nanjing, Jiangsu 210016, China

Note: This paper is part of the APL Photonics Special Topic on State-of-the-Art and Future Directions in Optical Frequency Comb Sources, Enabling Technologies, and Applications.
[a]**Author to whom correspondence should be addressed:** jijun.he@nuaa.edu.cn; danzhu@nuaa.edu.cn; and pans@nuaa.edu.cn

ABSTRACT

Wideband radio frequency (RF) channelization is essential for the reception and detection of cross-band RF signals in various applications, including communications, radar, and spectrum sensing. However, digital channelizers are inefficient at performing RF channelization over a working bandwidth above 10 GHz. Meanwhile, current photonic RF channelizers face challenges in simultaneously considering a wideband, multi-channel, and a high crosstalk suppression ratio. In this work, we proposed and demonstrated a wideband image-reject RF channelization scheme based on integrated dual-soliton microcombs. The dual-soliton microcombs are used for RF spectral copies and heterodyne detection, respectively. Supported by image-reject mixers, the RF channelization is verified with an 8–37 GHz working bandwidth, a 1.2 GHz channel bandwidth, and 25 channels. The image suppression ratio is higher than 34 dB for single-tone signals and 20 dB for wideband signals. Our approach provides an innovative architecture of integrated photonic RF channelizers with high performance, which can benefit a wide range of RF applications by miniaturizing the systems.

I. INTRODUCTION

The reception and detection of wideband radio frequency (RF) signals is a critical function in many scientific and technological fields, such as fast detection of vacant time gaps and frequency bands in integrated sensing and communication (ISAC),[1] real-time waveform feature extraction in cognitive radar,[2,3] electronic countermeasures,[4] and spectrum sensing.[5,6] Many of these applications necessitate the capability to slice a wideband RF signal into multiple narrow sub-bands for parallel reception to match the performance of the back-end digital signal processor (DSP), known as channelization. The traditional channelization is most often carried out by using an analog-to-digital converter (ADC) and subsequent DSP,[7,8] involving signal filtering and decimation in the digital domain. The bandwidth of this channelization scheme is significantly constrained by the sampling rate of the ADC. At present, the sampling rate of commercial ADCs is mostly below 10 GHz, which makes digital channelization unsuitable for RF signals above X-band without the aid of mixers.

The invention of the optical frequency comb (OFC) provides a new mentality for wideband RF channelization.[9–15] Profitting from the plentiful frequency components of the OFC, the multiple spectral copies of the RF signal are generated by modulating the RF signal onto the OFC. Channelization can be achieved using another OFC with a vernier frequency to downconvert the spectral copies or using optical filters with a periodic frequency response to filter the spectral copies. Therefore, the free spectral range (FSR) and the number of comb lines of the OFC determine the working bandwidth and the channel number of channelization, respectively. Electro-optic (E-O) combs have been used primarily for RF channelization because of their simplicity and flexibility.[16] However, a single E-O modulator produces no more than five comb lines,[17–23] which severely limits the

channel number. To overcome this, cascaded E-O modulators have been applied to extend the number of comb lines.[24–27] Despite this, the number of channels is still limited to only a dozen or so. In addition, due to the bandwidth limitation of the E-O modulator, the FSR of the E-O comb generally does not exceed 40 GHz. When receiving high-frequency wideband signals is channelized, the overlap of the spectral copies is unavoidable. Therefore, an OFC with a much wider FSR and simultaneously more comb lines is key to improving the performance of channelization.

Recently, some approaches that allow for the creation of OFCs with ultra-wide FSRs spanning optical C–L bands have been applied in channelization, such as those based on shockwave parametric mixers[28–30] and micro-ring resonators (MRRs).[31–35] In Ref. 30, the parametric mixers were used to produce vernier OFCs with 18 comb lines, achieving the channelization with a 1.2-GHz channel bandwidth in the frequency range of 15.5–37.1 GHz. Nevertheless, the use of multiple E-O modulators and pump lasers makes the system structure complex and bulky, which is not the optimum selection for generating the OFCs in RF channelization applications. The emerging technique of MRR-based frequency combs (microcombs) exhibits many advantages (e.g., compact footprint and high coherence) over the conventional technique, which can benefit the RF channelization performance. For example, Tan *et al.* applied an active MRR and a passive MRR with quasi-matched FSRs to realize RF channelization with 8.08-GHz working bandwidth and 121.4-MHz channel bandwidth.[35] The active MRR yielded a microcomb, while the passive MRR acted as a periodic optical filter. Consequently, the spectral copies of wideband RF signals were generated by the microcomb, and the passive MRR filtered the corresponding spectral bins as output channels in the periodic passband. Despite this, to facilitate subsequent digital processing, the channelized output signal generally needs to be an intermediate frequency (IF). This scheme using homodyne detection does not achieve RF signal downconversion. In addition, the crosstalk suppression ratio is limited by the Q factor of the passive MRR, which is only 6.9 dB. Thus, it remains a challenge to achieve RF channelization with a wideband, multi-channel, and a high crosstalk suppression ratio simultaneously.

In this paper, we proposed and demonstrated a wideband image-reject RF channelization scheme. The proposed approach uses dual-MRRs with slight differences in radii to generate the main microcomb and the vernier microcomb, respectively. The main microcomb acts as the signal comb to generate spectral copies of RF signals, and the vernier microcomb acts as the local oscillator (LO) comb. After the selection of dense wavelength division multiplexers (DWDMs), image-reject mixers (IRMs) are used to slice the RF spectrum into a bank of narrow channels by heterodyne detection. In this scheme, the FSRs of both microcombs are near 100 GHz, ensuring that the working bandwidth of channelization reaches 50 GHz (double-sideband modulation) or 100 GHz (single-sideband modulation). The spectra of both microcombs cover the entire C-band, providing sufficient channel numbers. In addition, the IRM based on the balanced Hartley structure is used in this scheme.[36,37] It allows for the downconversion and suppression of undesired mixing spurs of RF signals in the analog domain, including the image interference and frequency doubling spurs, so that the scheme has a higher crosstalk suppression ratio without additional digital signal processing. Through the demonstrated experiments, the RF channelization with 8–37 GHz working bandwidth and 25 channels is carried out. The image rejection ratio is higher than 34 dB (single-tone signal) or 20 dB (1-GHz wideband signal). Therefore, the performance of the proposed scheme is well beyond the existing channelization methods and fulfills the advanced requirements of ISAC, cognitive radar, electronic countermeasures, and other applications.[1–6]

II. PRINCIPLE

The principles of the proposed wideband image-reject RF channelization are illustrated in Fig. 1. The schematics in Figs. 1(a) and 1(b) illustrate the spectra of the main microcomb and the vernier microcomb, respectively. It should be noted that the radii of the two MRRs that are used to generate the microcombs are designed to be slightly different, resulting in the repetition rates (f_{rep1} and f_{rep2}) of the microcombs being similar but not exactly equal. The spectra of the main microcomb $E_{\mathrm{main}}(t)$ and the vernier microcomb $E_{\mathrm{ver}}(t)$ are expressed as follows:

$$\begin{aligned} E_{\mathrm{main}}(t) &= \sum_{n=1}^{N} A_1(n)\exp\left[j2\pi(f_{c1}+nf_{\mathrm{rep1}})t\right], \\ E_{\mathrm{ver}}(t) &= \sum_{n=1}^{N} A_2(n)\exp\left[j2\pi(f_{c2}+nf_{\mathrm{rep2}})t\right], \end{aligned} \tag{1}$$

where A_1, A_2 and f_{c1}, f_{c2} denote the amplitudes and offset frequencies of the two microcombs, respectively. As can be seen, the two microcombs gradually walk off from each other and the vernier beat is $f_{\mathrm{ver}}(n) = f_{c2} - f_{c1} + n(f_{\mathrm{rep2}} - f_{\mathrm{rep1}})$, where n is the number of microcomb lines. The main microcomb is modulated by the signal under test (SUT), which can be equivalent to the frequency domain convolution of the spectra. The generated spectral copies are indicated in Fig. 1(c). After wavelength division multiplexing, the spectral copies and the vernier microcomb are selected and injected into the IRM, respectively, with the following expressions:

$$\begin{aligned} E_{\mathrm{sig}}(n,t) &= A_1(n)\gamma_{\mathrm{RF}}\exp\left[j2\pi(f_{c1}+nf_{\mathrm{rep1}}\pm f_{\mathrm{RF}})t\right] \\ &\quad + A_1(n)\gamma_{\mathrm{IM}}\exp\left[j2\pi(f_{c1}+nf_{\mathrm{rep1}}\pm f_{\mathrm{IM}})t\right], \\ E_{\mathrm{LO}}(n,t) &= \sum_{n=1}^{N} A_2(n)\exp\left[j2\pi(f_{c2}+nf_{\mathrm{rep2}})t\right]. \end{aligned} \tag{2}$$

It is assumed that the SUT contains an RF component (f_{RF}) and an image frequency component (f_{IM}). The γ_{RF} and γ_{IM} in Eq. (2) denote the E-O conversion loss of the RF signal and the image interference, respectively. Figure 2 shows the architecture of the IRM. The selected spectral copy and vernier comb line are injected into the signal port and the LO port of a 90° optical hybrid, respectively. The optical hybrid introduces phase shifts to E_{LO} and then outputs two in-phase ($I_1 = E_{\mathrm{sig}} + E_{\mathrm{LO}}$ and $I_2 = E_{\mathrm{sig}} - E_{\mathrm{LO}}$) and two quadrature ($Q_1 = E_{\mathrm{sig}} + jE_{\mathrm{LO}}$ and $Q_2 = E_{\mathrm{sig}} - jE_{\mathrm{LO}}$) optical signals. After balanced photoelectric detection, the output in-phase and quadrature signals (i_{I} and i_{Q}, respectively) can be expressed as

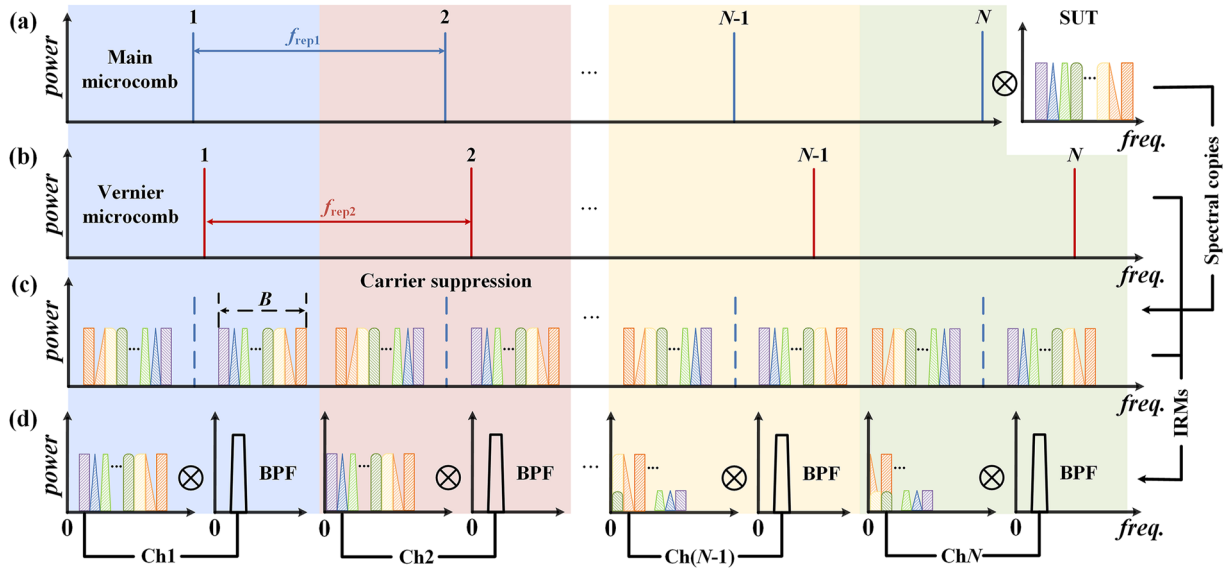

FIG. 1. Illustration of the principles of the proposed wideband image-reject RF channelization. (a) Spectral schematic of the main microcomb (left) and wideband RF signals (right). (b) Spectral schematic of the vernier microcomb. (c) Spectral copies generated by the frequency domain convolution of the main microcomb and SUT. (d) Simplified description of the image-rejection and the channel selection. SUT: signal under test, BPF: bandpass filter, IRM: image-reject mixer, and Ch: channel.

$$\begin{aligned} i_{\mathrm{I}}(t) &= I_1 I_1^* - I_2 I_2^* = 4A_1(n)A_2(n)\{\gamma_{\mathrm{RF}}\cos[2\pi(f_{\mathrm{RF}} - f_{\mathrm{ver}}(n))t] + \gamma_{\mathrm{IM}}\cos[2\pi(f_{\mathrm{ver}}(n) - f_{\mathrm{IM}})t] \\ &\quad + \gamma_{\mathrm{RF}}\cos[2\pi(f_{\mathrm{RF}} + f_{\mathrm{ver}}(n))t] + \gamma_{\mathrm{IM}}\cos[2\pi(f_{\mathrm{ver}}(n) + f_{\mathrm{IM}})t]\}, \\ i_{\mathrm{Q}}(t) &= Q_1 Q_1^* - Q_2 Q_2^* = 4A_1(n)A_2(n)\{\gamma_{\mathrm{RF}}\sin[2\pi(f_{\mathrm{RF}} - f_{\mathrm{ver}}(n))t] - \gamma_{\mathrm{IM}}\sin[2\pi(f_{\mathrm{ver}}(n) - f_{\mathrm{IM}})t] \\ &\quad - \gamma_{\mathrm{RF}}\sin[2\pi(f_{\mathrm{RF}} + f_{\mathrm{ver}}(n))t] - \gamma_{\mathrm{IM}}\sin[2\pi(f_{\mathrm{ver}}(n) + f_{\mathrm{IM}})t]\}. \end{aligned} \tag{3}$$

It can be seen that the mixing spurs ($f_{\mathrm{RF}} \pm f_{\mathrm{IM}}$) and frequency doubling spurs ($2f_{\mathrm{RF}}$ and $2f_{\mathrm{IM}}$) introduced by the RF signal and image interference mixing are eliminated through the balanced photoelectric detection. To suppress the image spurs and out-of-band spurs, the two outputs are coupled by a 90° bridge electrical hybrid and then filtered by a bandpass filter (BPF), as shown in Fig. 1(d). Finally, the output signal of the nth channel is derived as

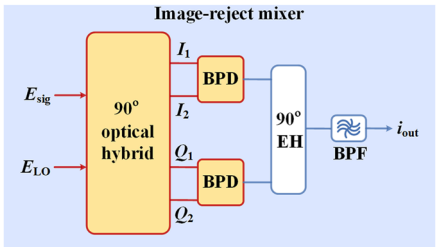

FIG. 2. Schematic of the image-reject mixer architecture. BPD: balanced photodetector, EH: electrical hybrid, and BPF: bandpass filter.

$$\begin{aligned} i_{\mathrm{out}}(t) &= \left[i_{\mathrm{I}}(t) + i_{\mathrm{Q}}(t)\angle 90^\circ\right] \otimes h_{\mathrm{BPF}}(t) \\ &= 8A_1(n)A_2(n)\gamma_{\mathrm{RF}}\sin\{2\pi[f_{\mathrm{RF}} - f_{\mathrm{ver}}(n)]t\}, \end{aligned} \tag{4}$$

where $h_{\mathrm{BPF}}(t)$ indicates the impulse response function of the BPF. As can be seen, only the difference frequency of the RF signal and the vernier beat is output, while the image spurs and other undesired spurs are eliminated. When $f_{\mathrm{RF}} - f_{\mathrm{ver}}(n)$ falls in the BPF passband, the RF signal will be successfully channelized in the nth channel. Thanks to the two soliton microcombs and IRMs, the proposed scheme achieves RF channelization with a wideband, multi-channel, and a high crosstalk suppression ratio.

III. EXPERIMENTAL RESULTS AND DISCUSSIONS

The experimental setup is illustrated in Fig. 3(a). To generate the desired soliton microcombs, two high Q-factor Si_3N_4 MRRs on separate chips are used in the experiment. MRR1 with a designed radius of 227 μm generates the main microcomb with an FSR of 98.55 GHz, while MRR2 with a designed radius of 226 μm generates the vernier microcomb with an FSR of 99.70 GHz. The pump generated by a CW laser (Toptica Photonics CTL 1550) is split into two

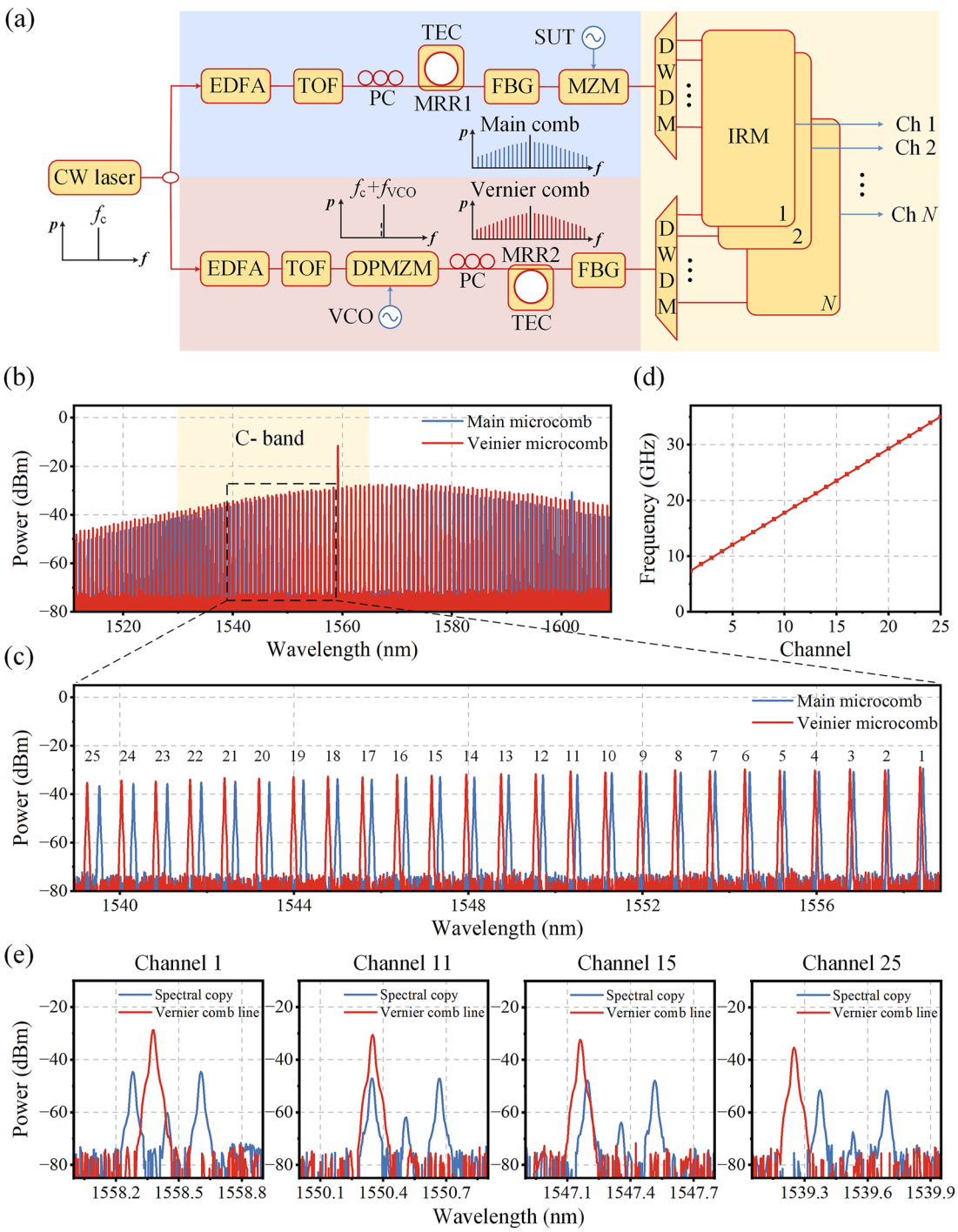

FIG. 3. Experimental setup of the wideband image-reject RF channelization based on dual-soliton microcombs. EDFA: erbium-doped fiber amplifier, TOF: tunable optical filter, PC: polarization controller, DPMZM: dual parallel Mach–Zehnder modulator, VCO: voltage-controlled oscillator, TEC: thermo-electric cooler, MRR: micro-ring resonator, FBG: fiber Bragg grating, MZM: Mach–Zehnder modulator, SUT: signal under test, DWDM: dense wavelength division multiplexer, IRM: image-reject mixer, and Ch: channel. (b) Main microcomb spectrum (blue) and vernier microcomb spectrum (red). The dashed region indicates the comb lines applied for channelization. (c) Zoom-in of the spectra in the dashed region spanning 19.2 nm. (d) Vernier beats f_{ver} of channels 1–25. (e) Spectral copies (blue) and vernier comb lines (red) for channels 1, 11, 15, and 25, when the SUT is a single tone at 20 GHz.

branches, which are first amplified by erbium-doped fiber amplifiers (EDFAs, Keopsys CEFA-C-PB-HP) to 500 mW, and then, the noise is filtered out by tunable optical filters (TOFs, EXFO XTM-50-S) in each branch. The upper branch pump is injected directly into MRR1, while the lower branch pump is single-sideband frequency-shifted by a dual parallel Mach–Zehnder modulator (DPMZM, EOSPACE IQ-0DKS-25) driven by a voltage-controlled oscillator (VCO, AT-VCO-0510A-20) and then injected into MRR2. Both of the MRRs reach the single soliton state simultaneously by adjusting the pump wavelength, the VCO voltage, and the temperature of two thermo-electric coolers (TECs). After the generation of soliton microcombs, two wavelength tunable fiber Bragg gratings (FBGs) are applied to reduce the pump power. Figure 1(b) shows the spectra of the main microcomb and the vernier microcomb after FBGs, which are measured using an optical spectrometer (Yokogawa AQ6370D). In this experiment, 25 microcomb lines are selected in the dashed region for RF channelization with 25 channels. As shown in Fig. 3(c), the main microcomb and the vernier microcomb walk off from each other, spanning 19.2 nm.

To accurately measure the working bandwidth of the RF channelization, the vernier beats of 25 channels are detected using a high-speed photodetector (Finisar XPDV3120R, 70 GHz) after filtering and coupling two microcombs. Figure 3(d) shows the vernier beats of 25 channels, increasing linearly from 7.40 to 35.05 GHz. Subsequently, the SUT is modulated onto the main microcomb using a Mach–Zehnder modulator (MZM, EOSPACE AZ-DV-65) working at the minimum point to generate spectral copies. After two DWDMs, the spectral copy and the vernier comb line used for the same channel are selected and then fanned out to the IRM, respectively. It should be noted that limited by the number of IRMs available, a pair of TOFs are used in the experiment to mimic the function of the DWDMs, and the performance of each channel is verified in turn. When the SUT is a single tone at 20 GHz, the spectral copy and the vernier comb line for channels 1, 11, 15, and 15 are shown in Fig. 3(e). The BPF with 1–2.2 GHz passband is applied for the IMR in the experiment. Therefore, based on Eq. (4), the SUT will be downconverted to 1.17 GHz and output at the 11th channel.

To verify the ability of wideband RF channelization and the performance of image-rejection, the experiments of RF channelization for two-tone signals are carried out. The frequency components of the two-tone signal are set to $f_{\mathrm{ver}}(n)$ + 1.36 GHz and $f_{\mathrm{ver}}(n)$ − 1.84 GHz and generated by two RF signal generators (R&S SMA100B), respectively. As a result, both frequency components fall within the passband of the BPF after channelization. For example, the vernier beat of channel 1 $f_{\mathrm{ver}}(1)$ is 7.40 GHz, so the frequencies of the SUT are 8.76 GHz (RF signal) and 5.56 GHz (image interference). In the six experiments carried out, the frequencies of the SUTs are shown in the blue and red dots in Fig. 4(a), and the measured image suppression ratios of the different channels are shown in the green dots in Fig. 4(a). Figures 4(b)–4(g) present the channelized output spectra of the SUTs at channels 1, 5, 15, 20, and 25, which are measured using a spectrum analyzer (R&S FSWP). It can be seen that the proposed channelizer achieves the high-performance image interference suppression within 25 channels, and the image suppression ratios are higher than 34 dB. In addition, channel 1 and channel 25 achieve channelized reception of 8.76-GHz frequency component and 36.41-GHz frequency component, respectively, indicating that the working bandwidth of the proposed channelization reaches 8–36 GHz. It should be noted that the main reason for the decrease in the image suppression ratio in Figs. 4(b)–4(g) is the decrease in the signal-to-noise ratio (SNR) of the comb lines. Through reducing the microresonator losses or the dispersion engineering,[38,39] the conversion efficiency of microcombs can be improved, so the working bandwidth and the channel number of the proposed scheme are expected to be further enhanced.

The performance of the channelization of wideband RF signals also is experimentally investigated. Two linear frequency modulation (LFM) signals with different center frequencies are generated as SUTs using an arbitrary waveform generator (AWG, Keysight M8195A). The bandwidth, period, and duty ratio of the two LFM signals are set as 1 GHz, 1 μs, and 0.9, respectively. To mimic the RF signal and the image interference, the center frequencies of the two LFM signals are set as $f_{\mathrm{ver}}(n)$ + 1.6 GHz and $f_{\mathrm{ver}}(n)$ − 1.6 GHz, respectively. As a result, the channelized output spectrum of both LFM signals is 1.1–1.2 GHz. Figure 4(h) shows the channelized output spectrum of two LFM signals with center frequencies of 9.00 GHz (RF signal) and 5.80 GHz (image interference), respectively, at channel 1. As can be seen, the image suppression ratio of channel 1 is 24.27 dB within the 1-GHz bandwidth. Figure 4(i) shows the comparison of the channelized output time–frequency diagrams with and without image rejection. The left diagram in Fig. 4(i) is the result of direct detection of the spectral copy and the vernier comb line on channel 1 by a PD, while the right one is the result of image-reject mixing using IRMs. It can be seen that the application of IRM effectively suppresses wideband image interference and ensures the crosstalk suppression ratio of the proposed channelization to be good enough. Figures 4(j) and 4(k) show the channelized output spectrum and time–frequency diagram of two LFM signals with center frequencies of 10.16 and 6.96 GHz at channel 2, respectively. The image suppression ratio of channel 2 reaches 20.15 dB. Limited by the performance of the AWG, the experiments of the wideband image-reject RF channelization are carried out on channels 1 and 2.

To better verify the performance of the proposed RF channelizer under strong image interference, the channelization of dual QPSK signals is experimentally carried out. The dual QPSK signals are generated by the AWG with carrier frequencies of 9.26 GHz (QPSK1) and 12.46 GHz (QPSK2), respectively. In addition, the baud rate of the dual QPSK signals is 1×10^7 sym/s. For channel 1, QPSK1 is the RF signal to be received, while QPSK2 is the out-of-band spur. Figure 5(a) shows the channelized output spectra of the dual QPSK signals from channel 1. Since QPSK2 falls outside the BPF passband after downconversion, it almost does not affect the channelized output of QPSK1. As shown in Fig. 5(b), the error vector magnitude (EVM) and constellation of the channelized output from channel 1 are acquired using a spectrum analyzer (Keysight E4440A) with an 80-MHz analysis bandwidth. The measured EVM of the channelized output from channel 1 is 12.55%. For channel 4, the carrier frequencies of downconverted or channelized QPSK1 and QPSK2 are the same, of which both are 1.6 GHz. Therefore, QPSK2 is the RF signal to be received, while QPSK1 is the in-band image interference on channel 4. In contrast to the out-of-band spur on

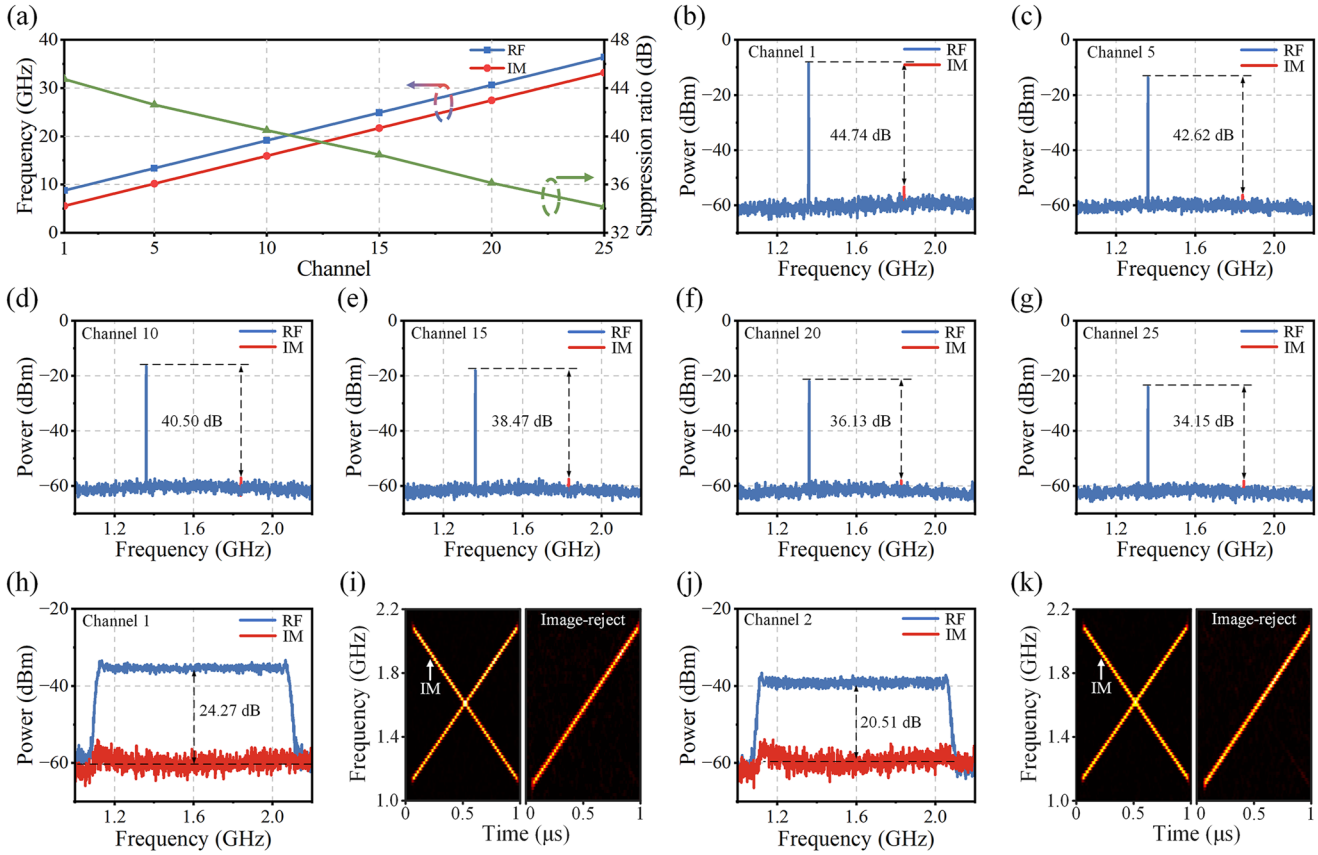

FIG. 4. Experimentally measured results of the wideband image-reject RF channelization. (a) Set SUT frequencies (blue and red) and measured image suppression ratios (green) at different channels. The SUT is a two-tone signal, in which the higher frequency component acts as the RF signal (blue) and the other frequency component acts as the image interference (red). Channelized output spectra of the SUTs at (b) channel 1, (c) channel 5, (d) channel 10, (e) channel 15, (f) channel 20, and (g) channel 25. Channelized output spectra of the wideband SUT at (h) channel 1 and (j) channel 2. The wideband SUT contains two linear frequency modulation signals, which act as the RF signal (blue) and the image interference (red), respectively. Channelized output time–frequency diagrams of the wideband SUT without (left) and with (right) image rejection at (i) channel 1 and (k) channel 2.

channel 1, the in-band image interference has a more serious impact on the distortion of the RF signal.[40] The channelized output spectra of the dual QPSK signals from channel 4 are displayed in blue in Fig. 5(c). To investigate the image suppression ratio of channel 4, the AWG is controlled to output only QPSK2, and the channelized output spectra of channel 4 are shown in red in Fig. 5(c). It can be seen that the image suppression ratio of channel 4 for QPSK1 is higher than 25 dB. Figure 5(d) shows the EVM and constellation of the channelized output from channel 4, and the measured EVM is 14.95%, which is slightly higher than that of channel 1.

The linearity of the proposed channelization is evaluated by measuring the spurious-free dynamic range (SFDR) in the experiment. A two-tone RF signal with frequencies of 10.15 and 10.16 GHz is generated by the RF signal generators as the SUT. After channelization, the two-tone signal downconverted to 1.59 and 1.60 GHz is output from channel 2, and the generated components of third order intermodulation distortion (IMD3) are 1.58 and 1.61 GHz. The measured powers of the fundamental signal and IMD3 at different SUT powers are shown in Fig. 6. The noise floor measured at 1-Hz resolution bandwidth (RBW) is −115 dBm/Hz, and the calculated SFDR is 90 dB/Hz$^{2/3}$, which can be further improved by reducing the optical link noise and optimizing the signal-to-noise ratio of the used soliton microcombs.

In summary, the proposed scheme achieves RF channelization with a wideband, multi-channel, and a high crosstalk suppression ratio simultaneously. Table I shows the performance comparison between this work and the state-of-the-art photonic RF channelizers. It can be seen that this work achieves a significantly wider working bandwidth and higher channel number compared to channelization schemes based on E-O combs.[17,18,20,25] Meanwhile, this work guarantees an excellent image suppression ratio within the working bandwidth, overcoming the key performance limitation of the RF channelizers based on the shockwave parametric mixers[30] and the MRR filtering.[35] It should be noted that in the field of coherent signal reception processing,[18,41] the soliton microcombs are better phase-locked to reduce the phase noise of the channelized signal,

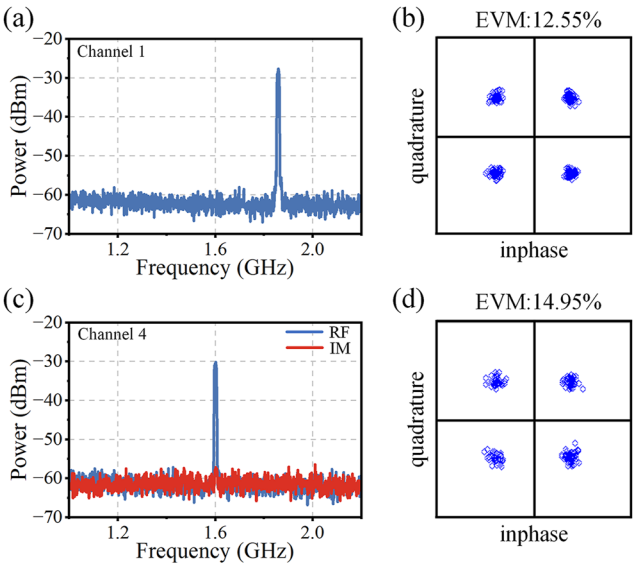

FIG. 5. Experimentally measured results of dual QPSK signal channelization. Channelized output spectra of the dual QPSK signals from (a) channel 1 and (c) channel 4. Measured EVM and constellation of the channelized output from (b) channel 1 and (d) channel 4.

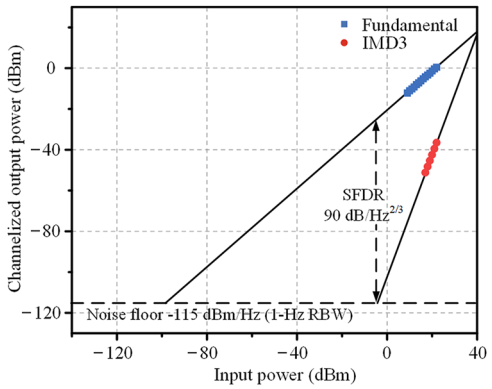

FIG. 6. Measurement results of spurious-free dynamic range (SFDR) on channel 2, with two-tone RF frequencies of 10.15 and 10.16 GHz. IMD3: third order intermodulation distortion and RBW: resolution bandwidth.

through phase locked loop and servos.[42,43] In addition, the cost, size, and weight of the system need to be further reduced for practical applications. This challenge is expected to be addressed by using the dual-output IRM to enhance comb efficiency,[17,44] employing the wavelength selective switch (WSS) to improve the flexibility of channel selection,[45,46] or utilizing the compact in-phase and quadrature receiver to reduce the device size.[47,48] Recent developments in programmable multifunctional integrated photonics[49,50] and optoelectronic heterogeneous integration[51,52] enable the integration of microwave photonic devices, such as 90° optical hybrids[53] and BPDs.[54] In particular, the iteration of the integrated microwave photonic filter subverts the bulkly fiber-based optical filter,[55] which lays a foundation for the miniaturization of the proposed RF channelizer on a chip.

TABLE I. Performance comparison with the state-of-the-art photonic RF channelizers. OFC-FSR: free spectral range of optical frequency comb, WBW: working bandwidth, CBW: channel bandwidth, CN: channel number, and ISR: image suppression ratio.

Reference	OFC-FSR (GHz)	WBW (GHz)	CBW (GHz)	CN	ISR (dB)
17	26, 27	7.5–10.5	1	2	≥25 (wideband)
18	24, 25	13–18	1	5	≥22 (wideband)
20	24	8.5–26	≤8	2	≥48 (single tone)
25	16, 20	2–14	1	12	≥26 (wideband)
30	200	15.5–37.1	1.2	18	NA
35	49	1–9 or 9–18	0.087	92	6.9 (single tone)
This work	98.55, 99.70	8–37	1.2	25	≥34 (single tone) ≥20 (wideband)

IV. CONCLUSION

In conclusion, the wideband image-reject RF channelization has been implemented using integrated dual-soliton microcombs. In the demonstration experiment, two soliton microcombs with the FSRs of 98.55 and 99.70 GHz spanning the optical C-band are generated as the main and vernier microcombs by the designed MRRs. Compared with the typical photonic RF channelization, the ultra-high FSRs ensure that the spectral copies of wideband RF signals do not overlap each other, enabling the working bandwidth of the proposed RF channelization to reach 8–37 GHz. In addition, the multiple comb lines of the soliton microcombs achieve the RF channelization with 25 channels in the experiment. The performance of the proposed RF channelization is investigated using different SUTs, such as two-tone signals, wideband LFM signals, and dual QPSK signals. The experimental results show that the image suppression ratio is higher than 34 dB for single-tone signals and 20 dB for 1-GHz wideband signals. When receiving the QPSK signals with image frequency interferences, the EVM of the channelized output signal still reaches 14.95%. The SFDR is also measured to be 90 dB/Hz$^{2/3}$ at last. Therefore, this work represents a significant advancement in the field of wideband RF channelization, featuring multi-channel, excellent crosstalk suppression, and a compact footprint. The proposed scheme not only paves the way for integrated RF channelizers but also reaffirms the revolutionary impact of microcomb technology on building a fully integrated photonic RF system.

ACKNOWLEDGMENTS

This work was supported in part by the National Key Research and Development Program of China under Grant No. 2022YFB2802700; in part by the Natural Science Foundation of Jiangsu Province under Grant Nos. BK20220887 and BK20220076; in part by the National Natural Science Foundation of China under Grant Nos. 62205145, 62271249, and 61971222; and in part by the Nanjing University of Aeronautics and Astronautics under Grant No. 3082022NS2022044.

AUTHOR DECLARATIONS

Conflict of Interest

The authors have no conflicts to disclose.

Author Contributions

J.D. and Y.W. contributed equally to this work.

Jiewen Ding: Conceptualization (equal); Investigation (equal); Methodology (equal); Writing – original draft (equal); Writing – review & editing (equal). **Yifan Wu**: Conceptualization (equal); Formal analysis (equal); Methodology (equal); Writing – original draft (equal); Writing – review & editing (equal). **Huashan Yang**: Methodology (equal). **Chao Zhang**: Methodology (equal). **Yifei Zhang**: Methodology (equal). **Jijun He**: Supervision (equal); Writing – review & editing (equal). **Dan Zhu**: Supervision (equal); Writing – review & editing (equal). **Shilong Pan**: Supervision (equal); Writing – review & editing (equal).

DATA AVAILABILITY

The data that support the findings of this study are available from the corresponding author upon reasonable request.

REFERENCES

[1] Y. Cui, F. Liu, X. Jing, and J. Mu, "Integrating sensing and communications for ubiquitous IoT: Applications, trends, and challenges," IEEE Network **35**, 158–167 (2021).

[2] Z. Zhang, Y. Liu, T. Stephens, and B. Eggleton, "Photonic radar for contactless vital sign detection," Nat. Photonics **17**, 791–797 (2023).

[3] D. Zhu and S. Pan, "Broadband cognitive radio enabled by photonics," J. Lightwave Technol. **38**, 3076–3088 (2020).

[4] R. Qiu, N. Guo, H. Li, Z. Wu, V. Chakravarthy, Y. Song, Z. Hu, P. Zhang, and Z. Chen, "A unified multi-functional dynamic spectrum access framework: Tutorial, theory and multi-GHz wideband testbed," Sensors **9**, 6530 (2009).

[5] T.-H. Yu, O. Sekkat, S. Rodriguez-Parera, D. Markovic, and D. Cabric, "A wideband spectrum-sensing processor with adaptive detection threshold and sensing time," IEEE Trans. Circuits Syst. I **58**, 2765–2775 (2011).

[6] H. Sun, A. Nallanathan, C.-X. Wang, and Y. Chen, "Wideband spectrum sensing for cognitive radio networks: A survey," IEEE Wireless Commun. **20**, 74–81 (2013).

[7] D. Gupta, T. V. Filippov, A. F. Kirichenko, D. E. Kirichenko, I. V. Vernik, A. Sahu, S. Sarwana, P. Shevchenko, A. Talalaevskii, and O. A. Mukhanov, "Digital channelizing radio frequency receiver," IEEE Trans. Appl. Supercond. **17**, 430–437 (2007).

[8] I. V. Vernik, D. E. Kirichenko, V. V. Dotsenko, R. Miller, R. J. Webber, P. Shevchenko, A. Talalaevskii, D. Gupta, and O. A. Mukhanov, "Cryocooled wideband digital channelizing radio-frequency receiver based on low-pass ADC," Supercond. Sci. Technol. **20**, S323 (2007).

[9] A. Hermans, K. Van Gasse, and B. Kuyken, "On-chip optical comb sources," APL Photonics **7**, 100901 (2022).

[10] J. Capmany and D. Novak, "Microwave photonics combines two worlds," Nat. Photonics **1**, 319 (2007).

[11] X. Zou, B. Lu, W. Pan, L. Yan, A. Stöhr, and J. Yao, "Photonics for microwave measurements," Laser Photonics Rev. **10**, 711–734 (2016).

[12] S. Pan and J. Yao, "Photonics-based broadband microwave measurement," J. Lightwave Technol. **35**, 3498–3513 (2017).

[13] T. Fortier and E. Baumann, "20 years of developments in optical frequency comb technology and applications," Commun. Phys. **2**, 153 (2019).

[14] S. A. Diddams, K. Vahala, and T. Udem, "Optical frequency combs: Coherently uniting the electromagnetic spectrum," Science **369**, eaay3676 (2020).

[15] D. Drayss, D. Fang, C. Füllner, G. Lihachev, T. Henauer, Y. Chen, H. Peng, P. Marin-Palomo, T. Zwick, W. Freude, T. J. Kippenberg, S. Randel, and C. Koos, "Non-sliced optical arbitrary waveform measurement (OAWM) using soliton microcombs," Optica **10**, 888–896 (2023).

[16] A. Parriaux, K. Hammani, and G. Millot, "Electro-optic frequency combs," Adv. Opt. Photonics **12**, 223–287 (2020).

[17] W. Chen, D. Zhu, C. Xie, J. Liu, and S. Pan, "Microwave channelizer based on a photonic dual-output image-reject mixer," Opt. Lett. **44**, 4052–4055 (2019).

[18] Z. Tang, D. Zhu, and S. Pan, "Coherent optical RF channelizer with large instantaneous bandwidth and large in-band interference suppression," J. Lightwave Technol. **36**, 4219–4226 (2018).

[19] B. Chen, Y. Fan, Z. Tian, W. Wang, B. Kang, W. Jiang, and Y. Gao, "An ultra-wideband microwave photonic channelized receiver with zero-IF architecture," Appl. Sci. **10**, 30 (2019).

[20] J. Yang, Z. Zheng, Y. Bai, H. Xue, Z. Su, J. Ma, X. Song, X. Gao, X. Zhao, and S. Huang, "Broadband dual-channel channelizer based on a microwave photonic power tunable image rejection down-conversion," Opt. Express **30**, 31795–31805 (2022).

[21] J. Yang, R. Li, Y. Dai, J. Dong, and W. Li, "Wide-band RF receiver based on dual-OFC-based photonic channelization and spectrum stitching technique," Opt. Express **27**, 33194–33204 (2019).

[22] P. Wang, J. Qiu, L. Yang, B. Wei, J. Li, and X. Jin, "Microwave photonics-based channelized receiving and reconstruction for broadband RF signal," Microwave Opt. Technol. Lett. **64**, 1758–1764 (2022).

[23] C. Xie, D. Zhu, W. Chen, and S. Pan, "Microwave photonic channelizer based on polarization multiplexing and photonic dual output image reject mixer," IEEE Access **7**, 158308–158316 (2019).

[24] F. Shi, Y. Fan, B. Ma, J. Zhang, X. Wang, J. Ge, W. Zhang, W. Zhai, and Y. Gao, "A microwave photonic channelized receiver with self-interference cancellation," J. Lightwave Technol. **41**, 627–636 (2022).

[25] W. Zhai, A. Wen, Y. Gao, D. Shan, and Y. Fan, "An ultraefficient broadband photonic channelizer based on polarization-division multiplexing and integrated dual-polarization coherent detection receiver," IEEE Trans. Microwave Theory Tech. **70**, 1821–1831 (2021).

[26] V. Torres-Company and A. M. Weiner, "Optical frequency comb technology for ultra-broadband radio-frequency photonics," Laser Photonics Rev. **8**, 368–393 (2014).

[27] X. Xie, Y. Dai, K. Xu, J. Niu, R. Wang, L. Yan, and J. Lin, "Broadband photonic RF channelization based on coherent optical frequency combs and I/Q demodulators," IEEE Photonics J. **4**, 1196–1202 (2012).

[28] E. Myslivets, B. P. Kuo, N. Alic, and S. Radic, "Generation of wideband frequency combs by continuous-wave seeding of multistage mixers with synthesized dispersion," Opt. Express **20**, 3331–3344 (2012).

[29] B. P.-P. Kuo, E. Myslivets, V. Ataie, E. G. Temprana, N. Alic, and S. Radic, "Wideband parametric frequency comb as coherent optical carrier," J. Lightwave Technol. **31**, 3414–3419 (2013).

[30] A. Wiberg, D. Esman, L. Liu, J. Adleman, S. Zlatanovic, V. Ataie, E. Myslivets, B. P.-P. Kuo, N. Alic, E. Jacobs, and S. Radic, "Coherent filterless wideband microwave/millimeter-wave channelizer based on broadband parametric mixers," J. Lightwave Technol. **32**, 3609–3617 (2014).

[31] M. Zhang, B. Buscaino, C. Wang, A. Shams-Ansari, C. Reimer, R. Zhu, J. M. Kahn, and M. Lončar, "Broadband electro-optic frequency comb generation in a lithium niobate microring resonator," Nature **568**, 373–377 (2019).

[32] M. Zhang, C. Wang, R. Cheng, A. Shams-Ansari, and M. Lončar, "Monolithic ultra-high-Q lithium niobate microring resonator," Optica **4**, 1536–1537 (2017).

[33] B. Shen, L. Chang, J. Liu, H. Wang, Q.-F. Yang, C. Xiang, R. N. Wang, J. He, T. Liu, W. Xie, J. Guo, D. Kinghorn, L. Wu, Q. X. Ji, T. J. Kippenberg, K. Vahala, and J. E. Bowers, "Integrated turnkey soliton microcombs," Nature **582**, 365–369 (2020).

[34] X. Xu, J. Wu, T. G. Nguyen, S. T. Chu, B. E. Little, R. Morandotti, A. Mitchell, and D. J. Moss, "Broadband RF channelizer based on an integrated optical frequency Kerr comb source," J. Lightwave Technol. **36**, 4519–4526 (2018).

[35]M. Tan, X. Xu, J. Wu, T. G. Nguyen, S. T. Chu, B. E. Little, R. Morandotti, A. Mitchell, and D. J. Moss, "Photonic radio frequency channelizers based on Kerr optical micro-combs," J. Semicond. **42**, 041302 (2021).
[36]D. Zhu and S. Pan, "Photonics-based microwave image-reject mixer," Photonics **5**, 6 (2018).
[37]D. Zhu, W. Chen, and S. Pan, "Photonics-enabled balanced Hartley architecture for broadband image-reject microwave mixing," Opt. Express **26**, 28022–28029 (2018).
[38]X. Xue, P.-H. Wang, Y. Xuan, M. Qi, and A. M. Weiner, "Microresonator Kerr frequency combs with high conversion efficiency," Laser Photonics Rev. **11**, 1600276 (2017).
[39]M. Rowley, P.-H. Hanzard, A. Cutrona, H. Bao, S. T. Chu, B. E. Little, R. Morandotti, D. J. Moss, G.-L. Oppo, J. S. Totero Gongora, M. Peccianti, and A. Pasquazi, "Self-emergence of robust solitons in a microcavity," Nature **608**, 303–309 (2022).
[40]B. F. Beidas, "Radio-frequency impairments compensation in ultra high-throughput satellite systems," IEEE Trans. Commun. **67**, 6025–6038 (2019).
[41]W. Hao, Y. Dai, Y. Zhou, F. Yin, J. Dai, J. Li, and K. Xu, "Coherent wideband microwave channelizer based on dual optical frequency combs," in *2016 IEEE Avionics and Vehicle Fiber-Optics and Photonics Conference* (IEEE, 2016), pp. 183–184.
[42]Y. Zhao, Z. Li, K. Zhou, X. Liao, W. Guan, W. Wan, S. Yang, J. Cao, D. Xu, S. Barbieri, and H. Li, "Active stabilization of terahertz semiconductor dual-comb laser sources employing a phase locking technique," Laser Photonics Rev. **15**, 2000498 (2021).
[43]I. Coddington, W. Swann, and N. Newbury, "Coherent dual-comb spectroscopy at high signal-to-noise ratio," Phys. Rev. A **82**, 043817 (2010).
[44]J. Ding, D. Zhu, B. Zhang, and S. Pan, "Dual-output filter-free microwave photonic single sideband up-converter with high mixing spur suppression," Appl. Opt. **60**, 7888–7893 (2021).
[45]Y. Ma, L. Stewart, J. Armstrong, I. G. Clarke, and G. Baxter, "Recent progress of wavelength selective switch," J. Lightwave Technol. **39**, 896–903 (2020).
[46]R. Kraemer, F. Nakamura, M. Van Den Hout, S. Van Der Heide, C. Okonkwo, H. Tsuda, A. Napoli, and N. Calabretta, "Multi-band photonic integrated wavelength selective switch," J. Lightwave Technol. **39**, 6023–6032 (2021).
[47]Y. Wang, X. Li, Z. Jiang, L. Tong, W. Deng, X. Gao, X. Huang, H. Zhou, Y. Yu, L. Ye, X. Xiao, and X. Zhang, "Ultrahigh-speed graphene-based optical coherent receiver," Nat. Commun. **12**, 5076 (2021).
[48]J. Zhou and Q. Zhang, "Multiple Tb/s coherent optical transceivers for short reach interconnect," IEEE J. Sel. Top. Quantum Electron. **28**, 8200814 (2022).
[49]D. Pérez, I. Gasulla, and J. Capmany, "Programmable multifunctional integrated nanophotonics," Nanophotonics **7**, 1351–1371 (2018).
[50]D. Marpaung, J. Yao, and J. Capmany, "Integrated microwave photonics," Nat. Photonics **13**, 80–90 (2019).
[51]C. Choi, H. Kim, J.-H. Kang, M.-K. Song, H. Yeon, C. S. Chang, J. M. Suh, J. Shin, K. Lu, B.-I. Park, Y. Kim, H. E. Lee, D. Lee, J. Lee, I. Jang, S. Pang, K. Ryu, S. H. Bae, Y. Nie, H. S. Kum, M. C. Park, S. Lee, H. J. Kim, H. Wu, P. Lin, and J. Kim, "Reconfigurable heterogeneous integration using stackable chips with embedded artificial intelligence," Nat. Electron. **5**, 386–393 (2022).
[52]D. Caimi, P. Tiwari, M. Sousa, K. E. Moselund, and C. B. Zota, "Heterogeneous integration of III–V materials by direct wafer bonding for high-performance electronics and optoelectronics," IEEE Trans. Electron Devices **68**, 3149–3156 (2021).
[53]K. Voigt, L. Zimmermann, G. Winzer, H. Tian, B. Tillack, and K. Petermann, "*c*-band optical 90° hybrids in silicon nanowaveguide technology," IEEE Photonics Technol. Lett. **23**, 1769–1771 (2011).
[54]P. Runge, G. Zhou, T. Beckerwerth, F. Ganzer, S. Keyvaninia, S. Seifert, W. Ebert, S. Mutschall, A. Seeger, and M. Schell, "Waveguide integrated balanced photodetectors for coherent receivers," IEEE J. Sel. Top. Quantum Electron. **24**, 6100307 (2017).
[55]Y. Liu, A. Choudhary, D. Marpaung, and B. Eggleton, "Integrated microwave photonic filters," Adv. Opt. Photonics **12**(2), 485–555 (2020).